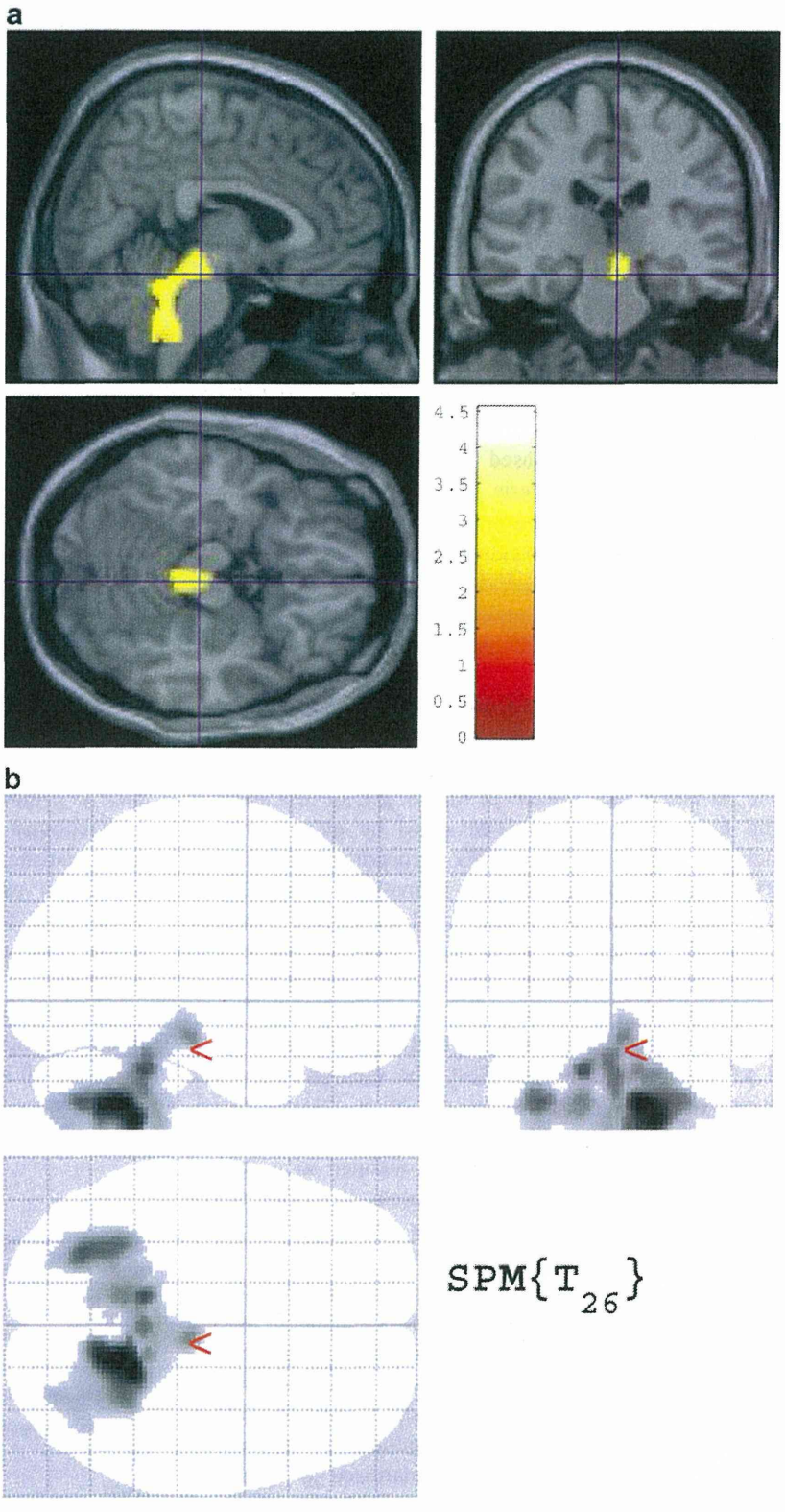

Fig. 1 Statistical parametric mapping (SPM) showing the negative correlation of the percentage of whole WM atrophy to that in various brain regions in the 30 DLB patients in group A

the averaged positive *Z* score in the target VOI with MRIcron (http://www.mccauslandcenter.sc.edu/mricro/mricron/). Using these averaged positive *Z* scores in the target VOI as a threshold, we used JMP 7.0 (SAS Institute, Cary, North Carolina) to determine receiver operating characteristic (ROC) curves for discriminating DLB and AD patients. The program

calculated the areas under the ROC curves (AUC; probability of concordance), sensitivity, specificity, and accuracy.

Results

DLB patients in group A exhibited a significant negative correlation of their percentage rate of significant whole WM atrophy with that of voxels in the right-side dominant dorsal midbrain, right-side dominant dorsal pons, and bilateral cerebellum and no significant positive correlations (Table 1, Fig. 1). The mean percentage rate of significant whole WM atrophy was 5.3±7.7 % (0–35.6). From this negative correlation, we determined a target VOI for DLB-specific atrophy. The target VOI was divided into three parts, and we created five target VOIs, consisting of the dorsal midbrain, dorsal pons, cerebellum, midbrain plus pons, and midbrain plus pons plus cerebellum (Fig. 2). ROC analysis using the averaged positive Z scores in these five target VOIs was performed to discriminate the DLB patients in group B from the AD patients (Fig. 3). A target VOI limited to the midbrain exhibited the highest AUC of 0.75, sensitivity of 80 %, specificity of 64 %, and accuracy of 72 %. A target VOI limited to the midbrain plus pons exhibited an AUC of 0.74, sensitivity of 60 %, specificity 90 %, and accuracy of 75 %. A target VOI limited to the pons exhibited an AUC of 0.68, sensitivity of 47 %, specificity of 93 %, and accuracy of 70 %. A target VOI limited to the cerebellum exhibited an AUC of 0.50, sensitivity of 20 %, specificity of 90 %, and accuracy of 55 %. A target VOI encompassing the midbrain plus pons and cerebellum exhibited an AUC of 0.55, sensitivity of 23 %, specificity of 90 %, and accuracy of 56.5 %.

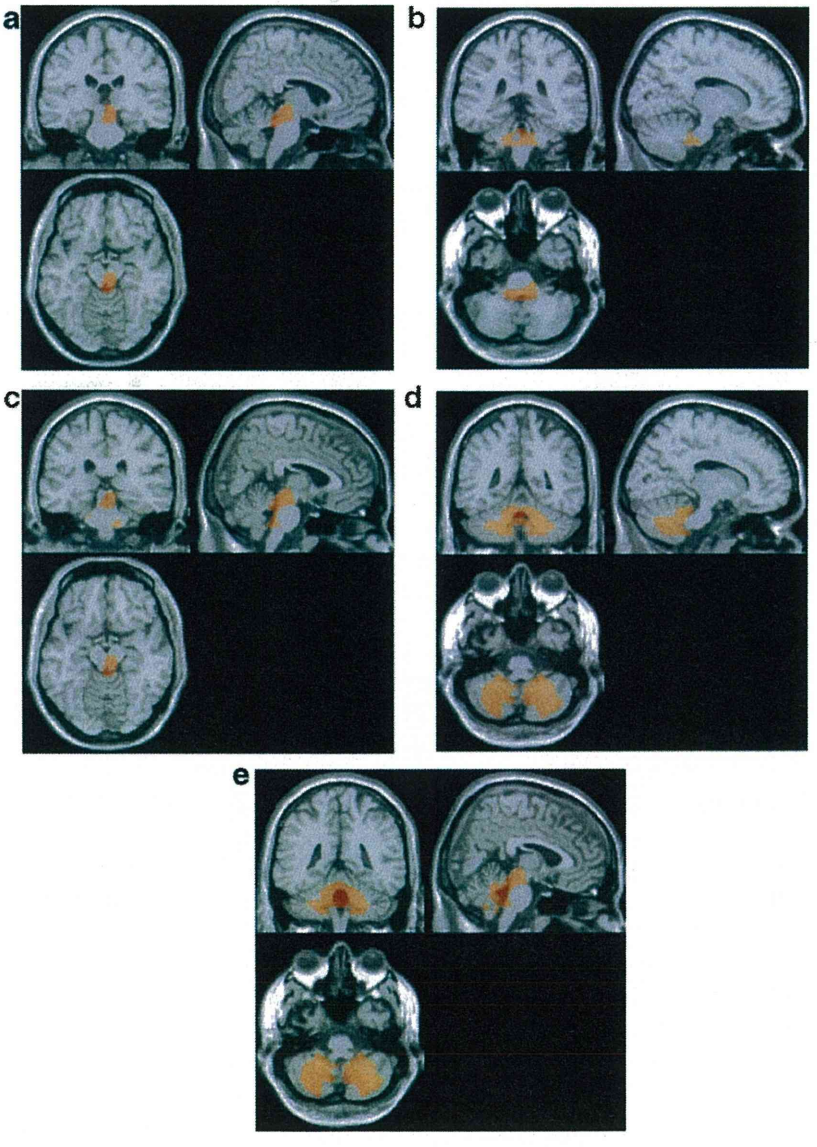

Fig. 2 Target volumes of interest (VOIs) for DLB-specific atrophy: **a** midbrain, **b** pons, **c** midbrain plus pons, **d** cerebellum, and **e** midbrain plus pons plus cerebellum

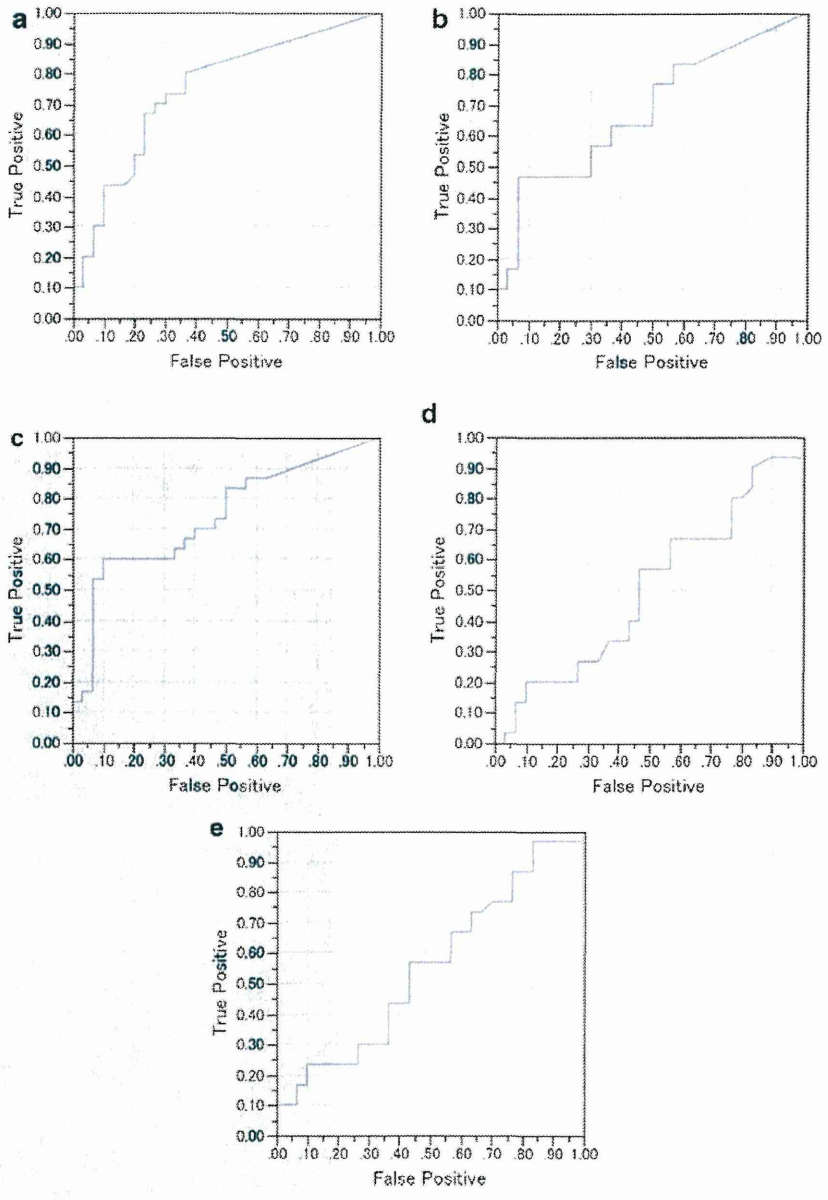

Fig. 3 ROC curves for discriminating DLB and AD patients using averaged positive *Z* scores in target VOIs as a threshold: **a** midbrain, **b** pons, **c** midbrain plus pons, **d** cerebellum, and **e** midbrain plus pons plus cerebellum

Discussion

The present study demonstrated DLB-specific WM atrophy in the right-side dominant dorsal midbrain, right-side dominant dorsal pons, and bilateral cerebellum. Right-side dominancy may result from the feature of the present cohort of DLB patients. The WM atrophy in these areas was more frequently observed in DLB than in AD. Of these areas, midbrain atrophy exhibited the most powerful discrimination of DLB and AD. These findings are consistent with pathological findings showing that Lewy bodies move up the brainstem into the midbrain and then to the forebrain before spreading into the cortex [18, 24, 25].

Takahashi et al. found no significant DLB-specific WM and GM atrophy compared to AD using SPM8 plus DARTEL [17]. Both our current study and theirs accepted an uncorrected threshold of $p<0.001$, but only ours used more stringent analysis of a cluster false discovery rate of $p<0.05$ for the multiple comparison correction. This inconsistency might arise from the differences in the cluster analyses or variability in the clinical cohorts (e.g., dementia severity, symptom presentation) of DLB and AD, although age and MMSE scores did not differ significantly in the two studies.

Distinguishing DLB from AD is important for choosing appropriate treatments, because clinical symptoms are sometimes too similar to distinguish between the two. Our ROC results showed that the use of VBM with SPM8 plus DARTEL may not be as accurate as using ^{123}I-MIBG myocardial scintigraphy [4]. This may be partly due to the fact that a majority of DLB patients have overlapping AD and DLB

pathologies. Thus, brain stem atrophy revealed by MRI may play a complementary role in determining the contribution of DLB and AD pathologies to the dementia syndrome.

Our study was possibly limited by several factors. Since we did not have MRI data of normal control group, we searched DLB-specific area for WM atrophy using a linear correlation analysis of each patient's WM image with significant atrophy rate for the whole brain WM as compared with "normal" database bundled with VSRAD. This indirect comparison between different MRI scanners should be validated in a further study based on the on-site normal database. Whether the present target VOI obtained from DLB versus normal is the best for DLB versus AD discrimination should be also further evaluated in direct comparison of a larger number of DLB and AD patients. However the present target VOI locates in the midbrain where DLB showed significant atrophy compared to AD in previous studies [12, 19]. We enrolled patients not only with probable DLB, but also those with possible DLB, even though their ^{123}I MIBG-SPECT results showed reduced H/M ratios on delayed phase images, and we did not assess the clinical severities (i.e., Hoehn and Yahr Scores) of the DLB patients. In the future, we intend to evaluate the usefulness of this target VOI for differentiating other dementia diseases using VBM with SPM8 plus DARTEL as well as the usefulness of combining this VBM analysis with other imaging modalities, including SPECT and PET and their relationship to the findings of postmortem neuropathology.

Conclusions

Our VBM analysis using SPM8 plus DARTEL demonstrated significant WM atrophy in the dorsal midbrain, dorsal pons, and cerebellum in the patients with DLB. Of these areas with DLB-specific WM atrophy, the midbrain atrophy exhibited the highest power for discriminating DLB from AD. This VBM approach may be useful for determining the contributions of DLB and AD pathologies to the dementia syndrome.

Conflict of interest We declare that we have no conflict of interest.

References

1. Zaccai J, McCracken C, Brayne C (2005) A systematic review of prevalence and incidence studies of dementia with Lewy bodies. Age Ageing 34:561–566
2. McKeith IG, Dickson DW, Lowe J et al (2005) Diagnosis and management of dementia with Lewy bodies: third report of the DLB Consortium. Neurology 65:1863–1872
3. Lippa CF, Duda JE, Grossman M et al (2007) DLB and PDD boundary issues: diagnosis, treatment, molecular pathology, and biomarkers. Neurology 68:812–819
4. Yoshita M, Taki J, Yokoyama K, Noguchi-Shinohara M, Matsumoto Y, Nakajima K, Yamada M (2006) Value of ^{123}I-MIBG radioactivity in the differential diagnosis of DLB from AD. Neurology 66:1850–1854
5. Treglia G, Cason E, Stefanelli A, Cocciolillo F, Di Giuda D, Fagioli G, Giordano A (2012) MIBG scintigraphy in differential diagnosis of Parkinsonism: a meta-analysis. Clin Auton Res 22:43–55
6. Small GW (2004) Neuroimaging as a diagnostic tool in dementia with Lewy bodies. Dement Geriatr Cogn Disord 17(suppl 1):25–31
7. Ishii K, Soma T, Kono AK, Sofue K, Miyamoto N, Yoshikawa T, Mori E, Murase K (2007) Comparison of regional brain volume and glucose metabolism between patients with mild dementia with Lewy bodies and those with mild Alzheimer's disease. J Nucl Med 48:704–711
8. Kono AK, Ishii K, Sofue K, Miyamoto N, Sakamoto S, Mori E (2007) Fully automatic differential diagnosis system for dementia with Lewy bodies and Alzheimer's disease using FDG-PET and 3D-SSP. Eur J Nucl Med Mol Imaging 34:1490–1497
9. Ashburner J, Friston KJ (2000) Voxel-based morphometry-the methods. NeuroImage 11(6 Pt1):805–821
10. Burton EJ, Karas G, Paling SM, Barber R, Williams ED, Ballard CG, McKeith IG, Scheltens P, Barkhof F, O'Brien JT (2002) Patterns of cerebral atrophy in dementia with Lewy bodies using voxel-based morphometry. NeuroImage 17:618–630
11. Burton EJ, McKeith IG, Burn DJ, Williams ED, O'Brien JT (2004) Cerebral atrophy in Parkinson's disease with and without dementia: a comparison with Alzheimer's disease, dementia with Lewy bodies and controls. Brain 127(Pt 4):791–800
12. Whitwell JL, Weigand SD, Shiung MM et al (2007) Focal atrophy in dementia with Lewy bodies on MRI: a distinct pattern from Alzheimer's disease. Brain 130(Pt 3):708–719
13. Cousins DA, Burton EJ, Burn D, Gholkar A, McKeith IG, O'Brien JT (2003) Atrophy of the putamen in dementia with Lewy bodies but not Alzheimer's disease: an MRI study. Neurology 61:1191–1195
14. Brenneis C, Wenning GK, Egger KE et al (2004) Basal forebrain atrophy is a distinctive pattern in dementia with Lewy bodies. NeuroReport 15:1711–1714
15. Hanyu H, Shimizu S, Tanaka Y, Hirao K, Iwamoto T, Abe K (2006) MR features of the substantia innominate and therapeutic implications in dementias. Neurobiol Aging 28:548–554
16. Ashburner J (2007) A fast diffeomorphic image registration algorithm. NeuroImage 38:95–113
17. Takahashi R, Ishii K, Miyamoto N, Yoshikawa T, Shimada K, Ohkawa S, Kakigi T, Yokoyama K (2010) Measurement of gray and white matter atrophy in dementia with Lewy bodies using diffeomorphic anatomic registration through exponentiated lie algebra: a comparison with conventional voxel-based morphometry. AJNR Am J Neuroradiol 31:1873–1878
18. Jubault T, Brambati SM, Degroot C, Kullmann B, Strafella AP, Lafontaine AL, Chouinard S, Monchi O (2009) Regional brain stem atrophy in idiopathic Parkinson's disease detected by anatomical MRI. PLoS One 4:e8247
19. Kantarci K, Ferman TJ, Boeve BF et al (2012) Focal atrophy on MRI and neuropathologic classification of dementia with Lewy bodies. Neurology 79:553–560
20. McKhann G, Drachman D, Folstein M, Katzman R, Price D, Stadlan EM (1984) Clinical diagnosis of Alzheimer's disease: report of the NINCDS-ADRDA work group under the auspices

of Department of Health and Human Services taskforce on Alzheimer's disease. Neurology 34:939–944
21. Jack CR Jr, Albert MS, Knopman DS, McKhann GM, Sperling RA, Carrillo MC, Thies B, Phelps CH (2011) Introduction to the recommendations from the National Institute on Aging-Alzheimer's Association workgroups on diagnostic guidelines for Alzheimer's disease. Alzheimers Dement 7:257–262
22. Matsuda H, Mizumura S, Nemoto K, Yamashita F, Imabayashi E, Sato N, Asada T (2012) Automatic voxel-based morphometry of structural MRI by SPM8 plus diffeomorphic anatomic registration through exponentiated Lie algebra improves the diagnosis of probable Alzheimer disease. AJNR Am J Neuroradiol 33:1109–1114
23. Hirata Y, Matsuda H, Nemoto K, Ohnishi T, Hirao K, Yamashita F, Asada T, Iwabuchi S, Samejima H (2005) Voxel-based morphometry to discriminate early Alzheimer's disease from controls. Neurosci Lett 382:269–274
24. Braak H, Ghebremedhin E, Rub U, Bratzke H, Del Tredici K (2004) Stages in the development of Parkinson's disease-related pathology. Cell Tissue Res 318:121–134
25. Jellinger KA (2004) Lewy body-related alpha-synucleinopathy in the aged human brain. J Neural Transm 111:1219–1235

Improved volumetric measurement of brain structure with a distortion correction procedure using an ADNI phantom

Norihide Maikusa[a)]
Integrative Brain Imaging Center, National Center of Neurology and Psychiatry, Tokyo 187-855, Japan

Fumio Yamashita
Iwate Medical University, Morioka 028-3694, Japan

Kenichiro Tanaka
Research Association for Biotechnology, Tokyo 105-0003, Japan

Osamu Abe
Department of Radiology, Nihon University School of Medicine, Tokyo 173-8610, Japan

Atsushi Kawaguchi
Biostatistics Center, Kurume University, Kurume 830-0011, Japan

Hiroyuki Kabasawa
Applied Science Laboratory, GE Healthcare, Tokyo 191-8503, Japan

Shoma Chiba
Research Association for Biotechnology, Tokyo 105-0003, Japan

Akihiro Kasahara
Imaging Center, The University of Tokyo Hospital, Tokyo 113-8655, Japan

Nobuhisa Kobayashi
Oizumi Hospital, Tokyo 178-0061, Japan

Tetsuya Yuasa
Department of Bio-systems Engineering, Graduate School of Science and Engineering, Yamagata University, Yonezawa 992-8510, Japan

Noriko Sato
Department of Radiology, National Center of Neurology and Psychiatry, Tokyo 187-855, Japan

Hiroshi Matsuda
Integrative Brain Imaging Center, National Center of Neurology and Psychiatry, Tokyo 187-855, Japan

Takeshi Iwatsubo
Department of Neuropathology, Graduate School of Medicine, The University of Tokyo, Tokyo 113-0033, Japan

The Japanese Alzheimer's Disease Neuroimaging Initiative

(Received 23 August 2012; revised 1 April 2013; accepted for publication 2 April 2013; published 28 May 2013)

Purpose: Serial magnetic resonance imaging (MRI) images acquired from multisite and multivendor MRI scanners are widely used in measuring longitudinal structural changes in the brain. Precise and accurate measurements are important in understanding the natural progression of neurodegenerative disorders such as Alzheimer's disease. However, geometric distortions in MRI images decrease the accuracy and precision of volumetric or morphometric measurements. To solve this problem, the authors suggest a commercially available phantom-based distortion correction method that accommodates the variation in geometric distortion within MRI images obtained with multivendor MRI scanners.

Methods: The authors' method is based on image warping using a polynomial function. The method detects fiducial points within a phantom image using phantom analysis software developed by the Mayo Clinic and calculates warping functions for distortion correction. To quantify the effectiveness of the authors' method, the authors corrected phantom images obtained from multivendor MRI scanners and calculated the root-mean-square (RMS) of fiducial errors and the circularity ratio as evaluation values. The authors also compared the performance of the authors' method with that of a distortion correction method based on a spherical harmonics description of the generic gradient design parameters. Moreover, the authors evaluated whether this correction improves the test–retest reproducibility of voxel-based morphometry in human studies.

Results: A Wilcoxon signed-rank test with uncorrected and corrected images was performed. The root-mean-square errors and circularity ratios for all slices significantly improved ($p < 0.0001$)

after the authors' distortion correction. Additionally, the authors' method was significantly better than a distortion correction method based on a description of spherical harmonics in improving the distortion of root-mean-square errors ($p < 0.001$ and 0.0337, respectively). Moreover, the authors' method reduced the RMS error arising from gradient nonlinearity more than gradwarp methods. In human studies, the coefficient of variation of voxel-based morphometry analysis of the whole brain improved significantly from 3.46% to 2.70% after distortion correction of the whole gray matter using the authors' method (Wilcoxon signed-rank test, $p < 0.05$).

Conclusions: The authors proposed a phantom-based distortion correction method to improve reproducibility in longitudinal structural brain analysis using multivendor MRI. The authors evaluated the authors' method for phantom images in terms of two geometrical values and for human images in terms of test–retest reproducibility. The results showed that distortion was corrected significantly using the authors' method. In human studies, the reproducibility of voxel-based morphometry analysis for the whole gray matter significantly improved after distortion correction using the authors' method.
 [http://dx.doi.org/10.1118/1.4801913]

Key words: Alzheimer's disease, magnetic resonance imaging, geometric distortion, image normalization

I. INTRODUCTION

Alzheimer's disease (AD) is the most common cause of dementia, and typically shows memory impairment at the earliest clinical stage. Magnetic resonance imaging (MRI) has shown much promise as a biomarker method of quantifying AD progression. Use of MRI in morphometric or volumetric measurement of brain atrophy, such as changes in cortical thickness, hippocampus volume, whole brain volume, voxel-based morphometry, or tensor-based morphometry, has resulted in improved diagnosis.[1–9] These measurements can also be used to assess the effectiveness of applied therapies.[10–12] A large multisite longitudinal study named the Alzheimer's Disease Neuroimaging Initiative (ADNI) was launched in the United States (US) in 2005.[13] A goal of the US-ADNI is to validate the MRI scan as a surrogate marker of AD. The Japanese Alzheimer's Disease Neuroimaging Initiative (J-ADNI) is another large multisite imaging study with the same goals as the US-ADNI.[14] Following the ADNI's study protocols, the J-ADNI recruited 150 elderly controls, 300 subjects with mild cognitive impairment, and 150 AD patients. Three-dimensional T1-weighted images were acquired from subjects and a specifically designed ADNI phantom (Phantom Laboratory, Salem, New York) was used to inspect image quality and artifacts as well as the stability of acquisitions.

MRI scans often contain geometrical distortions. The most prominent factors are image gradient nonlinearity, static magnetic field inhomogeneity, and magnetic susceptibility as typical image reconstruction relies on linear approximation of a magnetic field gradient.[15] A distortion can cause a superficial local volume change, which affects the precision and accuracy of volumetric and morphometric analysis.[13,15–19] The US-ADNI corrects image geometry for gradient nonlinearity using the gradwarp (GW) correction, which involves a gradient coil design and a phantom-based scaling correction method.[13,15] The former relies on the geometry of gradient coil construction and can only correct the nonlinear component of geometrical distortion. The latter corrects linear scaling changes of images through an affine transformation of nine degrees of freedom. However, GW correction requires information of the coil construction; the scanner is limited if this information is not available. Additionally, GW correction does not correct distortion variability between scanners or changes because of aging within the same scanner, and requires prior information of the gradient coil construction from the manufacture and is not available for all scanners.

On the other hand, several phantom-based distortion-correction methods have been reported in the literature.[16,17,20–22] Baldwin *et al.* characterized and corrected distortion using a three-dimensional (3D) grid phantom and elastic-body spline-kernel transformation function.[17] Carmanos *et al.* constructed a DUPLO-based phantom and proposed distortion correction using information characterized by that phantom and spherical harmonic expansion.[16] Schad *et al.*[20] carried out an early investigation on two-dimensional (2D) MRI distortion correction using a 2D polynomial equation. Menuel *et al.*[22] used phantom including cylindrical rods as fiducial points. Langlois *et al.* proposed a correction method based on the Fourier transform and a simple cubic phantom.[21] This method obtained information about distortion to allow correction of both gradient nonlinearity and background field inhomogeneity for many subsequent patients via scans of a phantom of well-known geometry. However, Gunter *et al.* reported that the distortion factor drifts.[19] Therefore, in a phantom-based method, it is desirable to periodically scan the phantom to correct the drift. The above studies used the phantom only to assess characteristics of the geometrical distortion.

In J-ADNI MRI scanning protocol, ADNI phantom images are acquired consecutively after patients are scanned in accordance with the US-ADNI protocol.[13] The ADNI phantom image was used to check the signal-to-noise ratio (SNR), contrast, and geometric distortion for all subjects at each scan time as done by the US-ADNI. Gunter reported that an ADNI phantom can be measured in a multisite study to identify scanner errors through central monitoring, and in the latest result, these errors would have contributed to imprecision in quantitative metrics of more than 25%.[19] The present report states

TABLE I. Range of parameters for MRI acquisition of human subjects and phantoms.

Manufacturer	Model name	Slice num	TR[a] (ms)	TI (ms)	Flip (deg)	Matrix [in-plane resolution (mm^2)]	Fov (mm^2)	Slice thickness (mm)	Plane
GE	GENESIS SIGNA SIGNA EXCITE SIGNA HDx/HDxt	166–180							
Siemens	Avanto MAGNETOM VISION Sonata Symphony Symphony Vision Symphony Tim	160	MA[b]:2400 BC[c]:3000	1000	8	192×192 [1.25×1.25] or 256×256 [0.9375×0.9375]	240×240	Human: 1.2 Phantom 1.3	Sagittal PE[d] = A/P
Toshiba	Excelart Vantage	180							
Philips	Achieva Intera	170	MA:2300						
Hitachi	ECHELON Vega	170	MA:2600	1100					

[a]TR is defined here as the receptition time for the inversion pulses.
[b]MA = multicoil phased-array head coil.
[c]BC = birdcage or volume head coil.
[d]PE is the phase encoding direction.

that ADNI phantom measurement is necessary to ensure consistency of MRI data acquired in a multisite longitudinal study like the ADNI project. If the distortion can be corrected using an ADNI phantom image, the correction can be applied to the ADNI protocol using the ADNI phantom that was already being employed for other purposes. In other words, the ADNI phantom-based distortion correction method can serve dual purposes: correction of geometrical distortion and monitoring of the scanner condition.

For the reason above, we suggest an ADNI phantom-based distortion correction using a polynomial equation to enhance the reliability and accuracy of structural analysis of brain images. Our method can correct nonlinear and linear components of geometrical distortion using the polynomial function. ADNI phantom scanning is available commercially and is recommended to monitor several MRI scanner conditions in multisite and longitudinal studies compliant with the ADNI study protocol. In this paper, we refer to this correction as the J-ADNI method. We evaluate the effectiveness of the method in terms of fiducial errors and circularity in phantom studies. For human studies, we use voxel-based morphometry (VBM). Finally, we compare improvements in distortion correction. Our method uses a commercially available phantom, and therefore attains distortion correction for all scanners without requiring information of the coil design from the manufacturer.

II. METHODS

II.A. MRI data and protocols

The pulse sequence used to acquire 3D, 1.5-T T1-weighted images was the magnetization-prepared rapid gradient echo (MPRAGE) sequence. MRI scanners were accepted via checking conformance with J-ADNI protocols, and we checked whether any image suffered serious degradation due to a motion artifact, warping around into the side of the skull, low SNR, signal loss, or metal artifact. This strengthened the longitudinal and cross-sectional analysis. The MPRAGE sequence is used to enhance gray/white contrast to noise for superior performance in applications requiring cortical segmentation.[13] We thus introduced the MPRAGE sequence to acquire magnetic resonance images in the J-ADNI. The parameters used to obtain magnetic resonance images with the MPRAGE sequence are listed in Table I for each manufacturer and model. For Siemens Magnetom Vision, Toshiba Excelart Vantage, and Hitachi Echelon Vega systems, a customized sequence designed to retain compatibility with the ADNI MPRAGE sequence was used. The parameters were chosen to be as close as possible to the parameters of the US-ADNI's MRI sequence to merge MRI data for global analysis and/or comparison of the population at a future date.

II.B. ADNI phantom design

The ADNI phantom contains 165 polycarbonate spheres filled with copper sulfate inside a water-filled clear urethane shell (20 cm in diameter). Four contrast spheres (3.0 cm in diameter) with copper sulfate concentrations of 0.9, 1.2, 1.7, and 2.4 mM provided scanner contrast. A large sphere (6.0 cm in diameter) containing 3.3 mM copper sulfate solution at the center of the phantom was used to calculate the SNR of a scanner and define the origin of the coordinate system. Inclusions (158 with diameters of 1.0 cm, and two with diameters of 1.5 cm) in 3.3 mM copper sulfate solutions, known as fiducial or small spheres, defined the geometrical coordinates of the phantom image in addition to

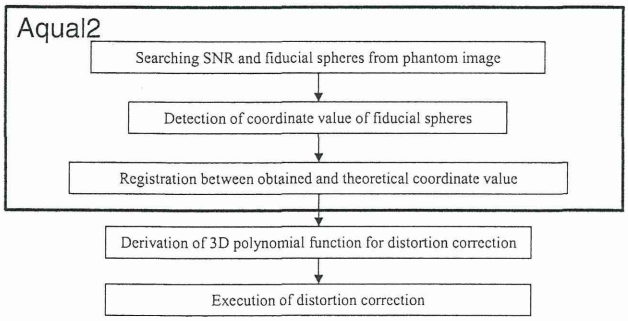

FIG. 1. Flowchart of distortion correction including mass-preservation resampling.

the SNR sphere. The phantom (Phantom Laboratory) was manufactured via numerous inspections of batches of both machined and molded components along with assembly inspections. The tolerance for the sphere locations was ±0.125 mm in the phantom's x–y directions (parallel to the equatorial plane) and ±0.3 mm in the z direction.

II.C. Method for correcting phantom-based geometrical distortion

A flow chart of the proposed distortion correction method is shown in Fig. 1. First, we performed phantom image analysis using Aqual2 (Acceptance Qualification tool), which was developed at the Mayo Clinic.[19] Aqual2 was written in MATLAB (MathWorks, Natick, Massachusetts) and is available via the Internet (http://adni.loni.ucla.edu/research/research-tools/aqual2/). This program finds 160 fiducial spheres and a SNR sphere to obtain coordinate values relative to the center of phantom images. The program is then able to register the obtained and designed coordinate values. By comparing the actual measured coordinate value of the fiducial and SNR spheres with the designed coordinate value, we can calculate the distortion field of the scanner. The warping function from a distorted coordinate to a design (i.e., nondistorted) coordinate value is given by

$$\begin{cases} X = \sum \sum \sum a_{pqr} x^p y^q z^r + \varepsilon \\ Y = \sum \sum \sum b_{pqr} x^p y^q z^r + \varepsilon \\ Z = \sum \sum \sum c_{pqr} x^p y^q z^r + \varepsilon \end{cases}, \quad (1)$$

where x, y, z and X, Y, Z are the obtained and designed coordinate values, respectively, along three orthogonal dimensions; p, q, and r are orders of the polynomial equation and n is the polynomial degree of a function; a_{pqr}, b_{pqr}, and c_{pqr} are coefficients of the polynomial equation; and ε is a Gaussian random variable. Because designed coordinate values of fiducial and SNR spheres are known, fiducial errors between design and obtained coordinate values reflect the geometric distortion of the scanner due to gradient nonlinearity, background field inhomogeneity, and magnetic susceptibility. We assume that the contribution of susceptibility in the ADNI phantom image is negligible. Thus, we can correct distortion in a MRI brain image for the same scanner using the equation derived from the phantom image. Note that our correction model has Gaussian distribution errors as described by ε in Eq. (1). Polynomial coefficients, a_{pqr}, b_{pqr}, and c_{pqr}, are calculated from the correspondence between x, y, z and X, Y, Z using Gaussian elimination to minimize Gaussian random variables in each of the three directions. Moreover, to use this polynomial equation, we must decide on the degrees of the polynomial (i.e., p, q, and r). To solve this problem, we use the Bayesian information criterion (BIC). The BIC is a criterion for model selection among a class of parametric models with different numbers of parameters.[23,24] In the present model, we assumed error variance between obtained and design sphere coordinate values given by a Gaussian distribution. The BIC is defined as

$$\mathrm{BIC}(n) = n \cdot \ln(\hat{\sigma}_e^2) + k \cdot \ln(n), \quad (2)$$

where σ is the error variance, n is the number of data points (i.e., the number of fiducial spheres), and k is the number of free parameters to be estimated. The best parameter of the polynomial equation is the one that minimizes Eq. (2). Hence, we selected an optimized set of polynomial functions for the three directions individually.

The polynomial function corrects geometrical distortion in a brain image, which is acquired immediately before phantom scanning with the same scanner. The resampling method used when an image is deformed to correct geometric distortion is trilinear interpolation. Additionally, it is necessary to correct the intensity to compensate for the change in effective voxel size with distortion. This intensity is corrected by multiplying the image intensity and the Jacobian determinant, $|J|$, calculated from the transformation equation at each voxel.[15,25] This equation is the polynomial function. We can calculate the Jacobian determinant, $|J|$, of the polynomial function associated with Eq. (1) as

$$|J| = \begin{vmatrix} \frac{\partial X'}{\partial x} & \frac{\partial X'}{\partial y} & \frac{\partial X'}{\partial z} \\ \frac{\partial Y'}{\partial x} & \frac{\partial Y'}{\partial y} & \frac{\partial Y'}{\partial z} \\ \frac{\partial Z'}{\partial x} & \frac{\partial Z'}{\partial y} & \frac{\partial Z'}{\partial z} \end{vmatrix}, \quad (3)$$

where $\partial/\partial x$, $\partial/\partial y$, and $\partial/\partial z$ are the partial derivative operators with respect to the orthogonal components, and X', Y', and Z' are the coordinates corrected by polynomial functions.

This correction software, written in MATLAB, executes automatically in about 15 min on a Xeon Processor E5540 (2.53 GHz) with RedHat Enterprise Linux 5.3 as the operating system using only input from phantom and brain images.

II.D. Evaluation metrics

For quantitative assessment of our correction method for phantom images acquired by all scanners ($n = 41$) at 38 J-ADNI clinical sites, we used two functions. The first function

was the root mean square (RMS) error in the determined location of fiducial spheres. The second function was the circularity ratio (CR) of an outer shell in a phantom image for three slices: axial, coronal, and sagittal. Polynomial functions for the correction procedure obtained from one phantom image were used to deform other phantom images acquired 1 week later by the same scanner.

To obtain RMS errors, coordinate values of fiducial spheres were acquired from uncorrected and corrected phantom images using Aqual2. We compared obtained and designed coordinate values, and calculated RMS errors of fiducial spheres.

Our method used geometrical information of the positions of fiducial spheres in phantom images. Therefore, it was expected that our method corrects distortion around the fiducial spheres. The overfitting of the distortion correction is not as great as predicted; accordingly, RMS errors are less than expected but the whole-image structures have unforeseen shapes. To assess the adequacy of the image obtained after distortion correction around fiducial points, we used the CR metric. The CR is defined as the amount of geometrical circle distortion according to Japanese industrial standards. The outer shell of a phantom is spherical and its orthogonal plane images are thus truly circular. Therefore, CRs of the outer shell in axial, coronal, and sagittal slices were used as other metrics to assess distortion. The CR is useful in assessing the validity of our method outside the fiducial sphere. The CR can be calculated as

$$\mathrm{CR} = \frac{r_i}{r_c}, \tag{4}$$

where r_i and r_c are radii of the incircle and circumcircle, respectively. If the ratio of the radii of the two concentric circles (incircle and circumcircle) is 1.0, the boundary is a true circle. To calculate the CR, we draw an incircle and circumcircle manually in three orthogonal images (i.e., the axial, sagittal, and coronal images) with origins at the center of the 3D phantom image. An operator carried out this task after only being instructed to draw two circles inscribed and circumscribed on the boundary between the outer shell of the phantom and background. To demonstrate the performance of our method, the Wilcoxon signed-rank test was performed for uncorrected and corrected images because the data may not be normally distributed because of the small sample size. A two-sided p-value less than 0.05 was considered statistically significant.

II.E. Comparison of geometrical distortion correction methods of the J-ADNI and US-ADNI

The US-ADNI employs the GW correction method[13] and ADNI phantom-based scaling correction. In GW correction, a set of spherical harmonic coefficients is computed for a particular gradient coil design, and can be used to correct the distortion arising from gradient nonlinearity embedded in acquired images.[18,25] Moreover, ADNI phantom-based linear scaling correction involves reducing the observed geometric drift or voxel size adjustment employing an affine transformation of nine degrees of freedom.[19] The parameters of affine transformation were acquired from design and obtained fiducial points of the ADNI phantom. Because the scaling correction program is not publicly available, we wrote MATLAB-based software for affine transformation of the magnetic resonance image using voxel size information obtained by Aqual2. We checked the adequacy of this program by comparing scaling corrected images available from the US-ADNI (www.loni.ucla.edu/ADNI/).

GW correction is only supported for scanners manufactured by GE and Siemens. GW correction uses the same spherical harmonic coefficients for the same gradient design to correct distortion only arising from gradient nonlinearity. Therefore, it cannot correct distortion variations between scanners of the same model or changes with time for the same scanner. These variations are generated by machine maintenance, such as magnetic field adjustment, repair of the magnetic coil, and quenching. We compared our proposed correction method with the GW method and the GW-plus-scaling method for corrected phantom images. Here, we need to separate out the contribution of gradient nonlinearity from other distortion components because our method corrects inhomogeneity in the magnetic background field as well as gradient nonlinearity. Bakker *et al.* reported that distortion only arose from gradient nonlinearity in the phase-encoding direction in a two-dimensional magnetic resonance image.[26] Subsequently, Baldwin *et al.* reported that the slice-encoding direction as well as the phase-encoding direction provides distortion when this principle is extended to a 3D magnetic resonance image.[17] Here, we assess RMS errors along the phase- and slice-encoding directions (i.e., the A/P and R/L directions, respectively), and also the CR in the axial image to compare the efficacy of our method with that of the GW and GW-plus-scaling correction procedures.

GW software is publicly available to researchers and we were able to obtain gradient information from GE Healthcare Japan, but we could only correct images acquired by GE MRI scanners using GW. For a statistical comparison of the J-ADNI, GW, and GW-plus-scaling correction methods, a Steel–Dwass signed-rank test was performed for the RMS error and CR.

II.F. Application of the distortion correction method to human studies

Geometrical distortion is induced by background field inhomogeneity and magnetic susceptibility as well as gradient nonlinearity. Magnetic susceptibility is dependent on the imaged object. Our method assumes that the contribution of susceptibility to geometrical distortion of the ADNI phantom image is negligible. Therefore, to evaluate our simple and practical method of correcting images of human subjects, we performed VBM analysis using software developed by Matsuda *et al.*[8] This approach allows us to automatically detect early specific atrophy in AD using three-dimensional T1-weighted MRI data as a series of segmentations using statistical parametric mapping 8 (SPM8) with the toolbox DARTEL. The following is a brief explanation of the procedure. Gray/white matter can be anatomically segmented employing